

# Suppression of Independent and Correlated Noise with Similarity-based Unsupervised Deep Learning

Chuang Niu<sup>a</sup>, Fenglei Fan<sup>a</sup>, Weiwen Wu<sup>a</sup>, Mengzhou Li<sup>a</sup>, Qing Lyu<sup>a</sup>, and Ge Wang<sup>a,1</sup>

<sup>a</sup>AI-based X-ray Imaging System (AXIS) Lab, Department of Biomedical Engineering, Rensselaer Polytechnic Institute, 110 8th Street, Troy, New York 12180, USA

This manuscript was compiled on December 22, 2024

**Denosing is one of the most important data processing tasks and is generally a prerequisite for downstream image analysis in many fields. Despite their superior denoising performance, supervised deep denoising methods require paired noise-clean or noise-noise samples often unavailable in practice. On the other hand, unsupervised deep denoising methods such as Noise2Void and its variants predict masked pixels from their neighboring pixels in single noisy images. However, these unsupervised algorithms only work under the independent noise assumption while real noise distributions are usually correlated with complex structural patterns. Here we propose the first-of-its-kind feature similarity-based unsupervised denoising approach that works in a nonlocal and nonlinear fashion to suppress not only independent but also correlated noise. Our approach is referred to as Noise2Sim since different noisy sub-images with similar signals are extracted to form as many as possible training pairs so that the parameters of a deep denoising network can be optimized in a self-learning fashion. Theoretically, the theorem is established that Noise2Sim is equivalent to the supervised learning methods under mild conditions. Experimentally, Noise2Sim achieves excellent results on natural, microscopic, low-dose CT and photon-counting micro-CT images, removing image noise independent or not and being superior to the competitive denoising methods. Potentially, Noise2Sim would open a new direction of research and lead to the development of adaptive denoising tools in diverse applications.**

Image denoising | Unsupervised learning | Low-dose CT denoising | Correlated noise

Image denoising is to recover signals hidden under a noisy appearance with numerous applications in many fields. Since noise is a statistical fluctuation governed by quantum mechanics, denoising is generally achieved by a mean/averaging operation. For example, local averaging methods can perform Gaussian smoothing (1), anisotropic filtering (2, 3), neighborhood filtering (4–6), and transform domain processing (7). On the other hand, nonlocal averaging methods use various nonlocal means with Gaussian kernel based weighting (8), or via nonlocal collaborative filtering in a transform domain (9, 10). Remarkably, the nonlocal methods usually outperform the local methods, as images usually consist of repeated patterns that can be leveraged in recovering signals coherently. Over the past several years, the area of image denoising has been dominated by deep convolutional neural networks (CNNs) (11). Different from the traditional methods that directly denoise an image based on an explicit model, the deep denoising methods optimize a deep neural network using training data, and then use the trained model to predict a denoised image, usually achieving better results with much less inference time than the traditional denoising methods.

The main stream deep denoising methods (12) require paired noise-clean images to train the networks, denoted as Noise2Clean. However, such noise-clean image pairs can be hardly obtained in real-world applications. To relax the requirement of paired noise-clean samples, Noise2Noise (13) was proposed to train a denoising network with paired noise-noise images that share the same content but are instantiated with independent noises. It is shown that Noise2Noise-based training tends to optimize a network up to the Noise2Clean quality under the assumption of zero-mean noise. However, the collection of paired noisy images is still expensive in many scenarios. To address this challenge, extensive efforts (14–22) were made to develop unsupervised learning methods that train a denoising network with single noisy images. Along this direction, Noise2Void (14) and Noise2Self (15) were proposed to predict the center pixel from its local neighbors, achieving promising results using single noisy images under the assumption of independent noises among neighbor pixels. However, these unsupervised deep denoising methods cannot suppress correlated noises, also referred to as structured noises, as they are predictable among neighbors. Since most noises to be handled in practical tasks are correlated with various textures, a general unsupervised denoising approach is highly desirable to unleash the power of deep learning for effective suppression of both independent and correlated noises, which is the holy grail of denoising methods.

Symmetry including similarity is ubiquitous in the physical world and naturally reflected in the image domain, featured by repeated or recursively embedded structures, edges, textures, etc., and plays an important role in modern science, engineering and medicine (23). However, there is currently no general approach to utilize similar features in images for unsupervised deep denoising. As the first effort to utilize similarity for unsupervised deep denoising, the initial version of Noise2Sim was shared on arXiv last year by our team (24). Somehow similar methods were heuristically designed for the same purpose (25, 26). Here we propose our Noise2Sim approach for similarity-based optimization of a deep denoising network with similar sub-images, and as a general framework for unsupervised deep denoising applicable to diverse cases. Importantly, in this article the Noise2Sim theorem is proved that under mild conditions the deep denoising network trained on similar sub-images is asymptotically equivalent to that trained in the supervised learning mode. In practice, the assumed conditions for the Noise2Sim theorem can be well tolerated in common tasks. Given the equivalency between Noise2Clean and Noise2Sim, the proposed unsupervised learning approach can, in principle, suppress both independent and correlated noises as effectively as the supervised deep denoising methods such as (27, 28).

The emphasis of this paper is on the general approach. Implementation details can be adapted in specific applications. For

example, several simple and efficient searching algorithms are adapted to extract similar sub-images in an application-specific fashion. Our extensive experiments on 2D natural and microscopy images, 3D low-dose computed tomography (CT) images, and 4D spectral CT images consistently show the superiority of Noise2Sim over both the traditional denoising methods and the deep denoising methods in terms of performance, efficiency, and practicality.

## Methods

**Supervised Deep Denoising.** A noisy image  $\mathbf{x}_i$  can be decomposed into two parts:  $\mathbf{x}_i = \mathbf{s}_i + \mathbf{n}_i$ , which is generated from the joint distribution  $p(\mathbf{s}, \mathbf{n}) = p(\mathbf{s})p(\mathbf{n}|\mathbf{s})$ , where  $\mathbf{s}_i$  and  $\mathbf{n}_i$  are the clean signal and associated noise respectively. A deep denoising method aims to learn a network function to recover the clean signal  $\mathbf{s}_i$  from the noisy signal  $\mathbf{x}_i$ , i.e.,  $\mathbf{y}_i = f(\mathbf{x}_i; \boldsymbol{\theta})$ , where  $f$  denotes the network function with a vector of parameters  $\boldsymbol{\theta}$  to be optimized. In a supervised training process (Noise2Clean), each noisy image  $\mathbf{x}_i$  is associated with the corresponding clean image  $\mathbf{s}_i$  as the target. Let  $\boldsymbol{\theta}_c$  be the network parameters optimized with paired noise-clean data, we have

$$\boldsymbol{\theta}_c = \arg \min_{\boldsymbol{\theta}} \frac{1}{N_c} \sum_{i=1}^{N_c} \|f(\mathbf{s}_i + \mathbf{n}_i; \boldsymbol{\theta}) - \mathbf{s}_i\|_2^2, \quad [1]$$

where  $N_c$  is the number of images, and the mean squared error (MSE) is used as the loss function (13, 14). Among all denoising methods, the supervised deep denoising methods achieve the best results but they are handicapped when paired images are unavailable.

**Noise2Sim.** The ubiquitous symmetry including similarity in the physical world leads to the well-known popularity of similar image pixels, patches, slices, volumes and tensors embedded within and across of images in different dimensionalities, which are conveniently referred to as similar sub-images in this study. Based on this observation, we propose Noise2Sim, a general unsupervised denoising approach for training a deep network without collecting paired noisy or clean target data. The key idea behind Noise2Sim is to replace explicit clean or noisy targets with the similar targets for training the denoising network, such that noises are suppressed to enhance signals faithfully. Specifically, given noisy images only, we first construct a set of similar sub-images, denoted by  $\mathbf{x}_i = \mathbf{s}_i + \mathbf{n}_i$  and  $\hat{\mathbf{x}}_i = \mathbf{s}_i + \boldsymbol{\delta}_i + \hat{\mathbf{n}}_i$ , where  $\boldsymbol{\delta}_i$  is the difference between the clean signal components in the similar sub-images, and  $\mathbf{n}_i$  and  $\hat{\mathbf{n}}_i$  are two different noise realizations. Let  $\boldsymbol{\theta}_s$  be the vector of network parameters optimized with the constructed similar pairs of data. We can find  $\boldsymbol{\theta}_s$  by minimizing the following loss function:

$$\boldsymbol{\theta}_s = \arg \min_{\boldsymbol{\theta}} \frac{1}{N_s} \sum_{i=1}^{N_s} \|f(\mathbf{s}_i + \mathbf{n}_i; \boldsymbol{\theta}) - (\mathbf{s}_i + \boldsymbol{\delta}_i + \hat{\mathbf{n}}_i)\|_2^2, \quad [2]$$

where  $N_s$  denotes the number of noisy similar image pairs. First of all, We present the following theorem to justify our Noise2Sim approach:

**Noise2Sim Theorem.** *Given the zero conditional expectations  $\mathbb{E}[\hat{\mathbf{n}}_i | \mathbf{s}_i + \mathbf{n}_i] = \mathbf{0}$  and  $\mathbb{E}[\boldsymbol{\delta}_i | \mathbf{s}_i + \mathbf{n}_i] = \mathbf{0}, \forall i$ , we have  $\lim_{N_s \rightarrow \infty} \boldsymbol{\theta}_s = \boldsymbol{\theta}_c$ .*

*Proof.* Let  $\mathbf{y}_i := f(\mathbf{s}_i + \mathbf{n}_i; \boldsymbol{\theta})$ , expanding the loss function in Eq. 2 and removing the terms that do not involve  $\boldsymbol{\theta}$ , we have

$$\begin{aligned} & \arg \min_{\boldsymbol{\theta}} \frac{1}{N_s} \sum_{i=1}^{N_s} \|\mathbf{y}_i - (\mathbf{s}_i + \hat{\mathbf{n}}_i + \boldsymbol{\delta}_i)\|_2^2 \\ &= \arg \min_{\boldsymbol{\theta}} \frac{1}{N_s} \sum_{i=1}^{N_s} (\|\mathbf{y}_i - \mathbf{s}_i\|_2^2 - 2\hat{\mathbf{n}}_i^T \mathbf{y}_i - 2\boldsymbol{\delta}_i^T \mathbf{y}_i). \end{aligned} \quad [3]$$

Clearly, the second and third terms respectively become

$$\begin{aligned} \lim_{N_s \rightarrow \infty} \frac{1}{N_s} \sum_{i=1}^{N_s} 2\hat{\mathbf{n}}_i^T \mathbf{y}_i &= 2\mathbb{E}[\hat{\mathbf{n}}_i^T \mathbf{y}_i] \\ \lim_{N_s \rightarrow \infty} \frac{1}{N_s} \sum_{i=1}^{N_s} 2\boldsymbol{\delta}_i^T \mathbf{y}_i &= 2\mathbb{E}[\boldsymbol{\delta}_i^T \mathbf{y}_i]. \end{aligned} \quad [4]$$

G. Wang originated the idea, initiated the project, and supervised the team. C. Niu designed specific algorithms and conducted all experiments. C. Niu and F. Fan established the mathematical analysis. W. Wu collected and preprocessed the photon-counting spectral micro-CT data. M. Li analyzed properties of CT noises. C. Niu and G. Wang drafted the manuscript, all co-authors participated discussion, contributed technical points, and revised the manuscript iteratively.

The authors declare no competing interest.

<sup>1</sup>To whom correspondence should be addressed. E-mail: wangg6@rpi.edu

Because

$$\begin{aligned}\mathbb{E}[\hat{\mathbf{n}}_i^T \mathbf{y}_i] &= \mathbb{E}[\mathbb{E}[\hat{\mathbf{n}}_i | \mathbf{y}_i]^T \mathbf{y}_i] = \mathbb{E}[\mathbb{E}[\hat{\mathbf{n}}_i | \mathbf{s}_i + \mathbf{n}_i]^T \mathbf{y}_i] = 0 \\ \mathbb{E}[\delta_i^T \mathbf{y}_i] &= \mathbb{E}[\mathbb{E}[\delta_i | \mathbf{y}_i]^T \mathbf{y}_i] = \mathbb{E}[\mathbb{E}[\delta_i | \mathbf{x}_i + \mathbf{n}_i]^T \mathbf{y}_i] = 0,\end{aligned}\tag{5}$$

where the second equivalence is due to the fact that  $\mathbf{y}_i = f(\mathbf{s}_i + \mathbf{n}_i; \boldsymbol{\theta})$  is deterministic. Hence, the following equations hold true:

$$\lim_{N_s \rightarrow \infty} \frac{1}{N_s} \sum_{i=1}^{N_s} 2\hat{\mathbf{n}}_i^T \mathbf{y}_i = 0 \quad \lim_{N_s \rightarrow \infty} \frac{1}{N_s} \sum_{i=1}^{N_s} 2\delta_i^T \mathbf{y}_i = 0.\tag{6}$$

Finally, as  $N_s \rightarrow \infty$ ,

$$\begin{aligned}\arg \min_{\boldsymbol{\theta}} \frac{1}{N_s} \sum_{i=1}^{N_s} \|\mathbf{y}_i - (\mathbf{s}_i + \hat{\mathbf{n}}_i + \delta_i)\|_2^2 \\ = \arg \min_{\boldsymbol{\theta}} \frac{1}{N_c} \sum_{i=1}^{N_c} \|\mathbf{y}_i - \mathbf{s}_i\|_2^2.\end{aligned}\tag{7}$$

That is,  $\lim_{N_s \rightarrow \infty} \boldsymbol{\theta}_s = \boldsymbol{\theta}_c$  □

**Remark 1:** One condition for the Noise2Sim theorem is the zero-mean conditional noise (ZCN),  $\mathbb{E}[\mathbf{n}'_i | \mathbf{s}_i + \mathbf{n}_i] = \mathbf{0}$ . This condition will be satisfied if similar sub-images have independent and zero-mean noises, i.e.,  $\mathbb{E}[\mathbf{n}'_i | \mathbf{s}_i + \mathbf{n}_i] = \mathbb{E}[\mathbf{n}'_i] = \mathbf{0}$ . As the direct current (DC) offsets in imaging systems are usually calibrated well, the expectation of observations is the real signal, meaning that the noise component has a zero mean. If noises of all pixels are independent from each other, the ZCN condition is directly satisfied, so the independent noises can be suppressed with Noise2Sim. In the case of correlated noises, if the distance between two sub-images is greater than the correlation length of noise, their noise components tend to be independent, as demonstrated in our experiments. Therefore, by learning between such nonlocal similar sub-images, it is feasible for the denoising network to perform well on correlated noises, based on the Noise2Sim theorem. It is worth to mention that there are no specific assumptions on the noise distribution. Hence, Noise2Sim can be adapted to process different noise distributions.

**Remark 2:** The other condition for the Noise2Sim theorem is the zero-mean conditional discrepancy (ZCD)  $\mathbb{E}[\delta_i | \mathbf{s}_i + \mathbf{n}_i] = \mathbf{0}$ . In practice, although the ZCD condition cannot be exactly satisfied, it is a very good approximation achieved by searching the intrinsically similar sub-images, as experimentally demonstrated in the Supporting Information (SI) Appendix S3.

**Remark 3:** Since the ZCN and ZCD conditions are practical, Noise2Sim can be regarded as an excellent surrogate of Noise2Clean or Noise2Noise without collecting paired training samples and yet with a wide range of applications. Moreover, Noise2Sim enjoys theoretical superiority over existing unsupervised deep denoising methods (14, 15, 26, 28). While these existing methods use training samples constructed only with local pixels, Noise2Sim works with similar sub-images selected globally in the entire image domain. The globality brings Noise2Sim distinguished advantages over its competing methods of locality; see SI Appendix S2 for detail analysis.

**Searching Similar Sub-Images.** Based on the Noise2Sim theorem, we need to search a set of similar sub-images from noisy images, with ZCN and ZCD conditions satisfied. Then, the denoising network can be optimized with the constructed similar training samples in a self-learning manner. Formally, a similar training set can be defined as  $\{(\mathbf{x}_i, \hat{\mathbf{x}}_i) | S(T(\mathbf{x}_i), T(\hat{\mathbf{x}}_i))\}$ , where  $T$  is a transform of each sub-image, and  $S$  is a metric to identify if two sub-images are similar or not. In practice,  $T$  and  $S$  may take different forms, depending on domain-specific priors. In this study, similar sub-images are similar pixels/patches in 2D images, slices in 3D images, and volumes in 4D images. Different searching algorithms are designed for various denoising applications; please read the SI Appendix S1 for more details.

## Results

To evaluate the practical performance of our approach, we applied Noise2Sim to various real-world applications, performing denoising tasks on 2D natural and microscopy, 3D low-dose computed tomography (LDCT), and 4D photon-counting spectral micro-CT images respectively. The Peak Signal-to-Noise Ratio (PSNR) (29) and Structural Similarity (SSIM) (30) metrics were used for quantitative evaluation. Here we mainly present our results of denoising correlated noises in LDCT and photon-counting spectral CT images, along with brief summaries of our denoising work in the cases of natural and microscopy images. More results are described in the SI Appendix, including the description of the datasets, network architectures, and implementation details.

**Application to Low-dose CT Images.** In the medical CT field, the radiation dose must be minimized according to the "As Low As Reasonably Achievable" (ALARA) guideline (31). Not surprisingly, the reduction of radiation dose will degrade the CT image quality and affect the diagnostic performance. To overcome this problem, great efforts have been made on LDCT reconstruction, also known as LDCT denoising, over the past two decades. Given the well-known successes of deep imaging (32), deep learning based methods recently became dominating in denoising LDCT images (33). In particular, Shan *et al.* demonstrated that the deep learning approach performs better than or comparable to the commercial iterative reconstruction methods in a double blind reader study (27). These methods work mainly in the supervised learning mode, assuming that the paired low-dose and normal-dose CT (NDCT) images are available. However, supervised LDCT image denoising requires either

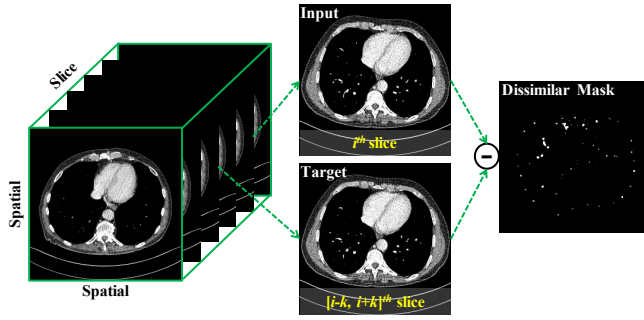


**Fig. 1.** Construction of training samples from 3D LDCT images. The similar slices along the longitudinal direction are selected to construct training samples, where the dissimilar pixels are identified with a mask image and excluded during training.

**Table 1. Comparison of denoising results using different methods on the Mayo dataset, where  $k$  was set to 2, and N2S\* means that the dissimilar masks were not used in the Noise2Sim training.**

Dataset	REDCNN	MAPNN	N2C	N2V	BM3D	N2S*	N2S
PSNR	28.59	28.47	28.78	23.36	27.28	27.81	<b>28.21</b>
SSIM	90.31	90.20	90.21	83.99	88.30	89.72	<b>90.22</b>

simulated noise insertion which does not reflect all the technical factors of a particular LDCT scan or the same patient scanned twice which is impractical in a clinical setting. To address this challenge, Noise2Sim was applied for LDCT image denoising using LDCT images only.

A volumetric CT image consists of two in-plane dimensions and one through-slice dimension, as shown in Fig. 1. It is well known that CT noise is spatially structured, which varies with the scanning protocol, reconstruction algorithm, patient conditions, scanner hardware, and so on. Geometrically, each detector row mainly contributes to one or several consecutive slices, and different detector rows are subject to independent noise realizations. As a result, there is a much weaker noise correlation between different slices (especially when the slices are well separated) than within the same slice. On the other hand, the same organ or tissue in a patient usually has the similar Hounsfield unit (HU) values. With these priors, similar slices with approximately independent and zero-mean noises can be obtained along the longitudinal axis of the patient. As shown in Fig. 1, given the  $i^{\text{th}}$  reference slice as input, a similar slice can be selected from the  $(i - k)^{\text{th}}$  to  $(i + k)^{\text{th}}$  slices, where  $k$  defines the searching range of similar slices, and used as the target during training. However, it cannot be guaranteed that the pixels at the same location in different neighbor slices are always similar to each other, especially when the structures are longitudinally changed. Hence, we specify dissimilar pixels (please see SI Appendix S1-C for details) between similar slices, as shown in Fig. 1, which are excluded when computing the loss during the training process.

With the above-described searching algorithm, we evaluated the Noise2Sim performance on the Mayo dataset for low-dose CT denoising in comparison with the popular supervised deep LDCT denoising methods RedCNN (33) and MAPNN (27). Table S7 and Fig. 2 show the numerical results and visual effects respectively. The quantitative results show that Noise2Sim achieves comparable PSNR results and even better SSIM results in comparison with the selected supervised learning methods, and significantly better than the competing unsupervised learning methods in terms of both metrics. Also, the performance of Noise2Sim was evidently degraded (N2S\* v.s. N2S in Table S7) if the dissimilar pixels were not excluded to violate the ZCD condition required by the Noise2Sim theorem. The visual results illustrate that Noise2Sim is better than RedCNN and MAPNN in preserving structural details, such as linear structures indicated with the yellow rows in Fig. 2 and textures within the yellow circles in Fig. 2, in reference to the normal-dose CT image. This is because Noise2Clean tends to remove noises aggressively while Noise2Sim tries to preserve informative details. It can be seen that Noise2Void does not work for structured CT noises, and the BM3D results are either over-smoothed or compromised with structured artifacts. In contrast, Noise2Sim produced excellent results for LDCT denoising.

In SI Appendix S5-F, we show that with a larger  $k$ , the noise dependence of similar pixels becomes weaker but similarity could become less and harder to detect. Overall, Noise2Sim has a strong power to control the denoising level with the neighborhood parameter  $k$ , as shown in Table S7 and Fig. S6 in SI Appendix. In our experiments,  $k = 2$  achieves the best trade-off between noise independence and feature similarity. In practice, the parameter  $k$  can be adjusted according to specific settings or down-stream tasks. Also,  $k$  could be automatically optimized if image quality can be quantitatively modeled, such as with a neural network and/or a Gram matrix (34).

**Application to Photon-counting Spectral Micro-CT Images.** As an emerging CT imaging technology, an x-ray photon-counting detector records individual photons and measures their energies accurately. This energy dependence information is potentially instrumental in enhancing dose efficiency, tissue characterization, and k-edge imaging (35). The data noise and artifacts remain

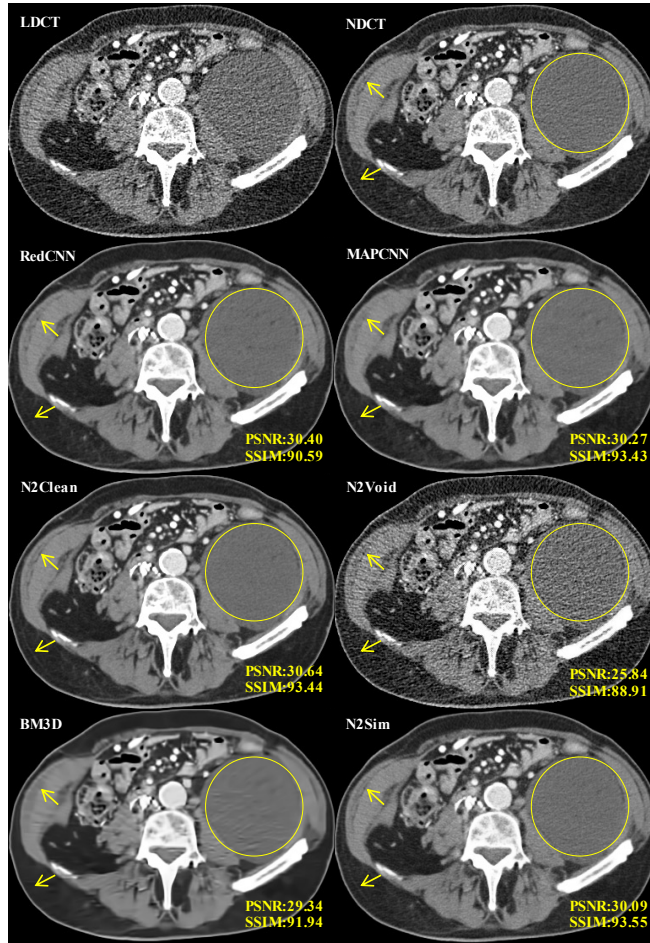


**Fig. 2.** Comparative results on the Mayo dataset, with the display window [-160, 240]HU, PSNR and SSIM values. The yellow arrows indicate that linear structures are better preserved using Noise2Sim. The textures within the yellow circles are similarly preserved in reference to the NDCT images.

challenging in photon-counting CT, caused by various factors especially a small number of photons received within narrow energy bins, the pile-up and charge-sharing effects, and so on (36). Because of the unavailability of clean data, supervised deep denoising methods cannot be used for photon-counting CT image denoising. Hence, we applied Noise2Sim to the case of photon-counting micro-CT image denoising. Additionally, Noise2Sim can be also used as the unsupervised deep prior in the reconstruction process, which is beyond the scope of this study.

A Spectral CT image tensor is of four dimensions, including three spatial dimensions (in plane and through slice), and a channel dimension, as shown in Fig. 3. Different from the searching method used for LDCT image denoising, for the  $i^{th}$  slice here we have a 3D tensor (two spatial and one spectral), a similar tensor is selected from  $(i - k)^{th}$  to  $(i + k)^{th}$  slices. An in-plane dissimilar mask is then computed as the filtered difference between two similar volumes as described in SI Appendix S1-C. After similar 3D tensors are extracted, the denoising network can be trained as an optimized map between similar tensors while ignoring the dissimilar spatial regions.

We evaluated the Noise2Sim method on a reconstructed photon-counting micro-CT image volume of a dead mouse scanned on a MARS spectral CT system; for more information, please see SI Appendix S4-A.5. Fig. 4 compares the results obtained using the representative unsupervised denoising methods. Again, Noise2Void did not work for denoising photon-counting micro-CT images due to highly correlated noise patterns. Although BM3D method suppressed structured noise, it produced either over-smoothed features (the 1<sup>st</sup> bin) or structured artifacts (the 5<sup>th</sup> bin). The main reason is that BM3D blindly removes high-frequency components in the transform domain according to the patch similarity. In this way, some fine structures are treated as noise and removed to address a large standard deviation prior, or some large structured noises are preserved to reflect a small standard deviation prior. In contrast, Noise2Sim accurately utilizes the intrinsic feature similarity of images and effectively suppresses structured noise after the deep denoising network is trained in a self-learning manner. As shown in Fig. 4, Noise2Sim achieved significantly better results in terms of noise suppression and anatomical fidelity. Practically, the denoising degree of Noise2Sim can be controlled by tuning the parameter  $k$  as described for LDCT image denoising, which can be optimized in specific applications. Moreover, we compared Noise2Sim with BM3D at different noise levels. Our data demonstrate that Noise2Sim is consistently better than BM3D (SI Appendix Fig. S7) and is much faster, up to three orders of magnitude (SI Appendix Table S6).

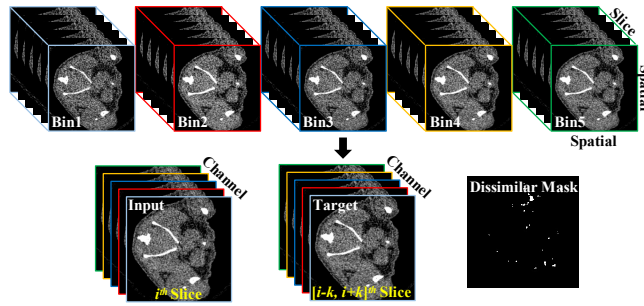


Fig. 3. Construction of training samples from 4D photon-counting micro-CT images. The similar volumes along the slice direction are selected to construct training samples, where the dissimilar vectors in a mask image are excluded during training.

Table 2. PSNR results obtained using different denoising methods on the BSD68 dataset corrupted by Gaussian noise at different levels. Std means the standard deviation of Gaussian noise.

Std	15	25	35	45	55	65
<i>N2Clean</i>	31.62	28.96	27.33	26.17	25.33	24.58
<i>N2Noise</i>	31.39	28.88	27.22	26.01	25.28	24.42
<i>N2Void</i>	29.26	27.72	26.61	25.36	24.84	23.95
<i>NLM</i>	29.92	27.58	26.07	24.95	24.06	23.29
<i>N2Sim</i>	<b>30.25</b>	<b>28.27</b>	<b>26.98</b>	<b>25.75</b>	<b>24.89</b>	<b>24.06</b>

**Application to Natural Images.** Natural image benchmark datasets are commonly used to evaluate the effectiveness of new denoising algorithms. For a fair comparison, we used the same datasets and network architecture as those used in the Noise2Void work (14), and independent Gaussian and Poisson noises were used. In the case of 2D images corrupted by independent noise, we propose an efficient two-step algorithm to construct a large set of similar sub-images from noisy images only; please refer to SI Appendix S1-A for a detailed description and Appendix S5-A,B,C for empirical analysis.

Let us first compared Noise2Sim with the Noise2Clean, Noise2Noise (13), Noise2Void (14), and NLM (8) methods in suppressing noises at different levels on the commonly used BSD68 and BSD400 datasets (11), as shown in Table 2. These results show that Noise2Sim is consistently better for a large range of noise levels  $15 \leq std \leq 65$  than the competing unsupervised methods. A representative visual example is in Fig. S4, showing that Noise2Sim produced higher quality denoising results than Noise2Void and NLM. Moreover, Table S5 and Fig. S4 in SI Appendix report the comparison results on more datasets including the BSD500 (37) and Kodak datasets, which were corrupted by either Gaussian or Poisson noises. These results support that the Noise2Sim method can effectively remove additive Gaussian noises and conditional Poisson noises in gray-scale and color images respectively. In Table S6, we compared Noise2Sim with closely relevant methods in terms of PSNR and inference time, including BM3D (10), Noise2Self (15), Noise2Same (16), and SNT (18) methods. Noise2Sim has the same inference time as Noise2Clean, Noise2Noise, and Noise2Void, directly taking the noisy image as input and outputting the denoised image without any additional processing. Although the classic BM3D method achieves the results comparable to the Noise2Sim counterparts, the inference time of BM3D is thousands times of that of Noise2Sim, which is consistent with what was reported in the Noise2Void paper (14). Therefore, Noise2Sim is both effective and efficient in general.

We further demonstrated that Noise2Sim can be adapted to denoise 2D images with correlated noises, where the smart phone images (38) were used for this purpose. In this case, we designed a searching algorithm for selection of similar patches to train deep networks as described in SI Appendix S1-B. The corresponding results are shown Fig. S5, showing that Noise2Sim removed structured noises in 2D images while Noise2Void did not work.

**Application to Microscopic Images.** We applied Noise2Sim to the fluorescence microscopic image datasets Fluo-C2DL-MSC (MSC) and Fluo-N2DH-GOWT1 (GOWT1), both of which only contain noisy images (39). In this study, the searching algorithm for similar images is the same as that used in the case of natural images. As mentioned earlier, when only noisy images are available without any target, the supervised deep denoising methods Noise2Clean and Noise2Noise are not applicable but Noise2Sim still works well. In (14), a limitation of the Noise2Void method was pointed out that Noise2Void cannot preserve grainy features when the local predictability is in question. Consistent to this well-known limitation, some grainy structures were missed in our reproduced Noise2Void results, as shown in the zoom-in regions in Fig. S4. In contrast, our Noise2Sim images well preserved structural subtleties, because self-similarity information is fully utilized in our denoising scheme.

## Discussion

In the Noise2Sim implementation, the key challenge is to find similar training samples satisfying the ZCN and ZCD conditions from noisy data without any labels. Specific to the dimensionality of involved images, several efficient searching algorithms have been presented for suppressing noises in this study. We believe that current algorithms can be further improved. For

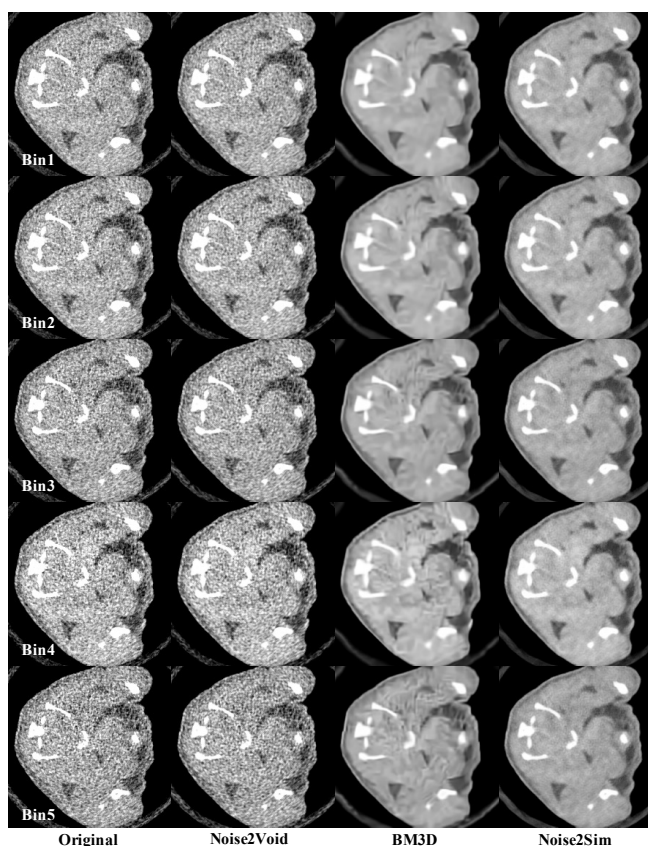


**Fig. 4.** Noise2Sim results on 4D photon-counting CT images. The 1<sup>st</sup>-4<sup>th</sup> columns are the original, Noise2Void, BM3D, and Noise2Sim images respectively. The 1<sup>st</sup>-5<sup>th</sup> rows are the reconstructed images from 1<sup>st</sup>-5<sup>th</sup> energy bins. The display window is  $[-300, 250]$  HU. The standard deviation for BM3D was set to 0.25.  $k$  was set to 5 for Noise2Sim. More comparative results can be found in SI at different denoising levels.

example, the discrete cosine transform we used for measuring similarity of image patches (SI Appendix S1-B) can be replaced by advanced transforms. Since here we focus on unsupervised learning, the commonly used UNet architecture and the Euclidean distance for similarity measurement were applied for a fair comparison. Clearly, the denoising performance should be better with a more advanced network design, more accurate similarity measurement, and a more suitable loss function.

As a general unsupervised denoising approach, Noise2Sim can be adapted to many other domains, not limited to the image domain, such as seismic data in geophysics and k-space data for MRI. In the general spirit of Noise2Sim, the deeper analysis of domain-specific data can help fully leverage similar data and achieve superior performance. For example, the LDCT denoising performance may be upgraded using a dual domain denoising network with similarity matches performed in the sinogram and image domains respectively. Moreover, due to its simplicity and efficiency, this approach can be incorporated into other frameworks as an intermediate step or a constraint. For example, Noise2Sim can be used as a deep prior in the CT image reconstruction process.

In conclusion, we have presented a novel similarity-based self-learning denoising approach only using noisy images with neither clean nor noisy paired labels. To our best knowledge, our approach is the first-of-its-kind to suppress either independent or structured noises in the unsupervised fashion. Theoretically, we have proved the Noise2Sim theorem that the similarity-based unsupervised method is equivalent to the supervised learning methods under mild conditions. Also, we have applied the Noise2Sim approach in various important applications to denoise 2D natural and microscopic images as well as 3D low-dose CT images and 4D photon-counting micro-CT images. Our experimental results have demonstrated the superiority and efficiency of the Noise2Sim approach in comparison with classic and existing deep learning denoising methods. Potentially, the Noise2Sim approach can be adapted to various domains for excellent denoising performance.

**Data Availability.** The datasets used in this study including Low Dose CT, BSD68, BSD500, Kodak, SIDD, and microscopy datasets, which can respectively be obtained through [www.aapm.org/grandchallenge/lowdosect/](http://www.aapm.org/grandchallenge/lowdosect/), [github.com/claasmichele/CBSD68-dataset](https://github.com/claasmichele/CBSD68-dataset), [www2.eecs.berkeley.edu/Research/Projects/CS/vision/bsds/](http://www2.eecs.berkeley.edu/Research/Projects/CS/vision/bsds/), [www.cs.albany.edu/~xypan/research/snr/Kodak.html](http://www.cs.albany.edu/~xypan/research/snr/Kodak.html), [www.eecs.yorku.ca/~kamel/sidd/](http://www.eecs.yorku.ca/~kamel/sidd/), [www.celltrackingchallenge.net/2d-datasets/](http://www.celltrackingchallenge.net/2d-datasets/). Source codes and private spectral photon-counting CT data are available at <https://github.com/niuchuangnn/noise2sim>.

**ACKNOWLEDGMENTS.** This work was supported in part by NIH/NCI under Award numbers R01CA233888, R01CA237267, R21CA264772, and NIH/NIBIB under Award numbers R01EB026646, R01HL151561, R01EB031102.

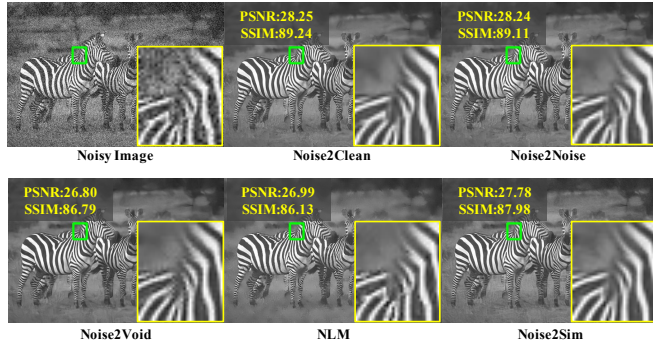


Fig. 5. Visual comparison of denoising results on the BSD68 dataset, with Gaussian noise  $Std = 25$ .

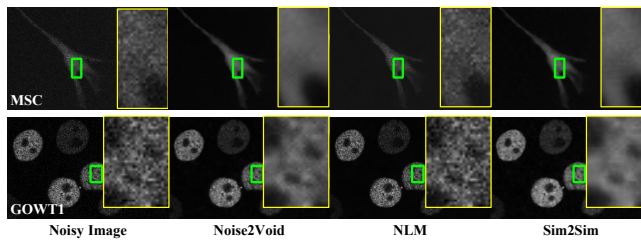
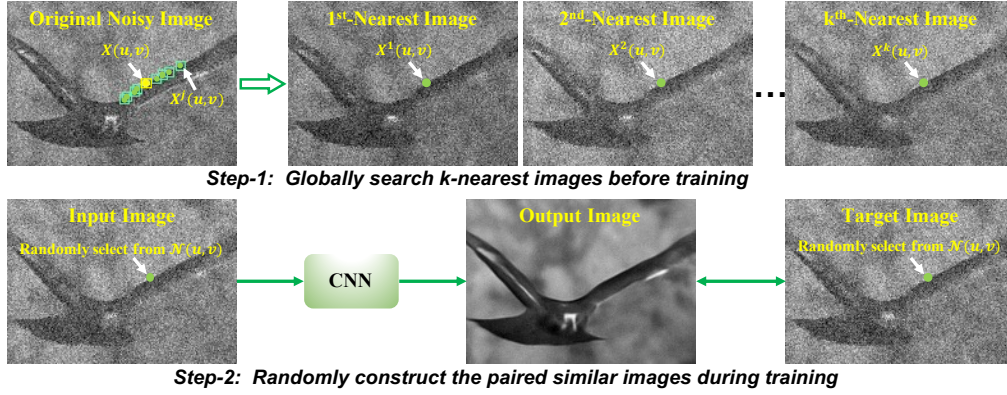


Fig. 6. Comparative results on GOWT1 and MSC datasets, which only contain noisy images so that *Noise2Clean* and *Noise2Noise* are not applicable. The yellow boxes show the zoom-in regions for visual inspection.

## S1. Searching Algorithms for Selection of Similar Sub-Images

As introduced in the main text, the similar training set is defined as  $\{(\mathbf{x}_i, \hat{\mathbf{x}}_i) | S(T(\mathbf{x}_i), T(\hat{\mathbf{x}}_i))\}$ , where  $T$  is the transformation function for sub-images, and  $S$  is the function to identify if two sub-images are similar or not. Here we describe the detail formulations for  $\mathbf{x}_i$ ,  $T$ , and  $S$  in different applications, including 2D images with independent noise, 2D images with correlated noise, and LDCT and photon-counting spectral micro-CT images.



**Fig. S1.** Construction of similar training samples for 2D images. Step 1 is to search for a set of  $k$  similar pixels for each pixel in the original noisy image, and form  $k$  most similar images, which is also referred to as nearest images. In the original noisy image, the yellow and green points respectively denote the reference pixel  $\mathbf{X}(u, v)$  and its  $k$  nearest pixels  $\mathbf{X}^j(u, v)$ ,  $j = 1, \dots, k$ , and the corresponding boxes present the patches respectively centered at these involved pixel that are used to compute the similarity of center pixels. The  $k^{\text{th}}$  nearest image is formed by replacing all pixels in the original noisy image with their  $k^{\text{th}}$  nearest pixels. Step 2 is to construct a pair of similar images as the input and the target to train a convolutional neural network (CNN). Each similar image is independently constructed by replacing every pixel  $\mathbf{X}(u, v)$  in the original noisy image with the pixel randomly selected from  $\mathcal{N}(u, v) = \{\mathbf{X}(u, v), \mathbf{X}^1(u, v), \dots, \mathbf{X}^k(u, v)\}$ , which are pre-computed in Step 1.

**A. 2D Images with Independent Noise.** In the case of independent noise, the sub-images  $\mathbf{x}_i$  are defined as pixels, and similar images are constructed by replacing original pixels with the searched similar pixels during training. For simplicity, here  $T$  is the identity function that means no transformations are applied to image pixels, and one can also use some transformations to reduce the variance of similarity estimation caused by noises (10). For the similarity estimation  $S$ , we adopt the  $k$ -NN strategy that each pixel is matched with  $k$  nearest similar pixels in terms of the Euclidean distance between their surrounding patches.

Specifically, let us describe this process at the pixel-level. For each reference pixel  $\mathbf{x}(u, v)$  with its coordinates  $(u, v)$  in a given noisy image  $\mathbf{x}$ , we compute its  $k$  nearest pixels over the whole image. The distance between two pixels  $\mathbf{x}(u_1, v_1)$  and  $\mathbf{x}(u_2, v_2)$  is defined as the Euclidean distance between their associated patches; i.e.,  $\|\mathcal{S}(u_1, v_1) - \mathcal{S}(u_2, v_2)\|_2$ , where  $\mathcal{S}(u, v)$  denotes a square patch that is determined by the pre-defined patch size and the center pixel  $\mathbf{x}(u, v)$ . Thus, each position in the image has a set of  $k + 1$  similar pixels (+1 means the reference pixel included), denoted as  $\mathcal{N}(u, v) = \{\mathbf{x}(u, v), \mathbf{x}^1(u, v), \dots, \mathbf{x}^k(u, v)\}$ , where  $\mathbf{x}^j(u, v)$  denotes the  $j$ -th nearest pixel relative to  $\mathbf{x}(u, v)$ . As shown in Fig. S1, the yellow and green dots denote the reference pixel and its nearest pixels, and the boxes are the associated patches. Based on these similar pixel sets, a similar noisy image can be constructed by replacing every original pixel  $\mathbf{x}(u, v)$  with a similar one randomly selected from  $\mathcal{N}(u, v)$ . Then, a pair of similar images is independently constructed in each iteration.

The number of all possible similar images to each given image is  $(k + 1)^{H \times W}$ , where  $H$  and  $W$  represent the image height and width respectively. If all similar images are prepared before training or on-the-fly during training, the memory space or computational time will be unacceptable. Naturally, we propose to divide the Noise2Sim training process into two steps. First, we generate  $k$ -nearest similar images from a single noisy image. The  $k$ -nearest similar images are obtained by sorting the  $k$ -nearest similar pixels for each pixel location, i.e., the  $j$ -th nearest image is  $[\mathbf{x}^j(u, v)]_{H \times W}$ , as shown in Fig. S1. Second, with these  $k + 1$  similar images, we randomly and independently construct a pair of similar images on-the-fly during training. The time searching for these similar images is acceptable in the first step, using an advanced algorithm on GPU. The construction of paired similar images takes little time in the second step. There are alternative ways to construct the training pairs, see SI C-B for comparative results. Also, since noise may harm the estimation of signal similarities, we propose to use the denoised image to improve the computation of the similarity between image patches, and then conduct Noise2Sim training again, which can be iterated if necessary; please see Subsection S5-B for details. In Subsection S5-A, we comprehensively studied the effects of the involved hyperparameters, the patch size and the neighborhood  $k$ .

**B. 2D Images with Correlated Noise.** To implement Noise2Sim for reducing correlated noises in 2D images, we divided each image into a set of small patches by sliding  $16 \times 16$  windows with a stride of 4 pixels. These small patches are regarded as the sub-images, and the deep denoising network is optimized by learning to map between similar patches. To evaluate the similarity between patches that are corrupted by correlated noises, we first convert the patches into the transform domain and removing the high-frequency components as in (10). Here we implement the transform function  $S$  as the discrete cosine transform (7). Then, the similarity is determined by the Euclidean distance between transformation coefficients. Finally, for each reference, 8 nearest patches were globally searched to construct the training set. During training, two similar patches were randomly selected to train the denoising network. The corresponding results are presented in subsection S5-E.

**C. LDCT CT Images and Photon-counting Micro-CT Images.** As introduced in Subsections **Application to Low-dose CT Images** and **Application to Photon-counting Spectral Micro-CT Images** in the main text, we search a similar image of a reference slice from its neighbor slices, i.e.,  $[i - k, i + k]^{\text{th}}$  slices,  $k$  defines the searching range. In particular, some pixels/vectors at the same in-plane location but on different slices may not be similar to each other when they represent different tissues or organs. According to the Noise2Sim theorem, these dissimilar parts will compromise the zero-mean conditional discrepancy condition, and thus should be excluded from training samples. Specifically, we denote a pair of similar LDCT images or spectral CT images as  $\mathbf{x}_i, \mathbf{x}_j \in R^{H \times W \times C}$ , where  $H, W, C$  denote height, width, and channel of CT images,  $C = 1$  for LDCT images, and  $i, j$  are the slice indices,  $j \in [i - k, i + k]$ . For each pair of vectors  $\mathbf{x}_i(u, v, :), \mathbf{x}_j(u, v, :) \in R^C$  at the same spatial location  $(u, v)$ , we use their surrounding patches to determine the similarity. The

patches of these two vectors share the same spatial coordinates  $S(u, v)$  that are determined by the spatial center  $(u, v)$  and the patch size  $s \times s$ . Formally, we define the distance map  $d \in R^{H \times W}$  between  $x_i$  and  $x_j$  as

$$d(u, v) = \frac{1}{s^2} \sqrt{\sum_{c=1}^C \left( \sum_{(p,q) \in S(u,v)} (x_i(p, q, c) - x_j(p, q, c))^2 \right)}. \quad [8]$$

In practice, the inner summation can be computed by the convolution with an  $s \times s$  kernel filled by ones. Then, the dissimilar mask  $m$  is computed as

$$m(u, v) = \begin{cases} 1 & d(u, v) > d_{th} \\ 0 & \text{otherwise} \end{cases} \quad [9]$$

where the  $d_{th}$  is a predefined threshold. In all experiments, we empirically set the patch size  $s = 7$  and the threshold  $d_{th} = 40$  in HU.

## S2. Comparison with Noise2Noise and Noise2Void



**Fig. S2.** Comparison of different deep denoising methods. *Noise2Clean* requires paired noise-clean samples. *Noise2Noise* takes paired noise-noise samples, which are easier to collect than *Noise2Clean* counterparts but still impractical in many scenarios. *Noise2Void* and *Noise2Self* predict a small portion of excluded pixels based on their neighbors in single noisy images during training. Different from these methods, *Noise2Sim* leverages self-similarity in a single noisy image and constructs training images using the noisy image itself in the same spirit of non-local means.

To better understand the advantages of *Noise2Sim*, here we further compare *Noise2Sim* with *Noise2Noise* and *Noise2void* methods. Fig. S2 shows the training samples used in different deep denoising methods in the case of 2D images with independent noises.

For *Noise2Noise*, paired noisy images, i.e.,  $x_i = s_i + n_i$  and  $x'_i = s_i + n'_i$ , are required to train the network, where  $n_i$  and  $n'_i$  are two independent and zero-mean noise realizations. The parameters  $\theta_n$  of the denoising network are optimized as

$$\theta_n = \arg \min_{\theta} \frac{1}{N_n} \sum_{i=1}^{N_n} \|f(s_i + n_i; \theta) - (s_i + n'_i)\|_2^2, \quad [10]$$

where  $N_n$  is the number of paired images for *Noise2Noise*. Theoretically, if the conditional expectation  $\mathbb{E}[n'_i | s_i + n_i] = 0$  is satisfied, the learned parameters  $\theta_n$  with paired noise-noise images will be equal to  $\theta_c$  optimized under paired noise-clean images as  $N_n \rightarrow \infty$  (40). As  $\hat{n}_i$  is independent to  $n_i$ ,  $\mathbb{E}[n'_i | s_i + n_i] = \mathbb{E}[n'_i | s_i] = 0$  is true under the zero-mean noise assumption. However, *Noise2Sim* cannot be applied when only single noisy images are available, while *Noise2Sim* still works well as demonstrated by our *Noise2Sim* theorem and experimental results.

For *Noise2Void*, only noisy images are required for network training. It splits the noisy image  $x_i$  into two parts, i.e.,  $x_i = x_i^c \cup x_i^r$ . As shown in Fig. S2,  $x_i^c$  contains a small set of pixels from  $x_i$  and used as the targets of the rest pixels  $x_i^r$ . Thus, the parameters  $\theta_v$  of the denoising network are optimized as follows:

$$\theta_v = \arg \min_{\theta} \sum_{i=1}^{N_v} \|f(x_i^r; \theta) - x_i^c\|_2^2, \quad [11]$$

Three assumptions are required to make the *Noise2Void* network work (14). First, the signal value is predictable from its local surrounding noisy pixels in the receptive field of the neural network. Second, the noise components of neighbor pixels are independent of each other. Third, the expectation of the noise component is zero, ensuring that the averaging operation gives the clean signal.

In contrast, the *Noise2Sim* theorem reveals that the similarity-based self-learning method is functionally equivalent to the paired learning methods *Noise2Noise* and *Noise2Clean*. Compared with *Noise2Void* and its variants, *Noise2Sim* has at least three advantages. First, in terms of the training samples, we have  $x_i^r \subset x_i$  and  $x_i^c \subset \hat{x}_i$ , so that *Noise2Sim* can be regarded as a non-local version of *Noise2Void*, leveraging both local and global information. Therefore, *Noise2Sim* enjoys principled superiority over *Noise2Void*. Second, since *Noise2Void* assumes that the signal is predictable from its neighbors, it cannot preserve grainy structures or isolated pixels that are irrelevant to their neighbors and thus are not predictable. Without relying on this signal predictability assumption, *Noise2Sim* does not suffer from this limitation and has the ability to preserve detailed structures as demonstrated in our experiments. Third, current unsupervised denoising methods cannot process correlated noises due to that they aim to map between neighbor noisy pixels during training while the correlated noises are also predictable. In contrast, *Noise2Sim* is a general approach that learns to map between paired similar training data, which can be constructed by adjacent or non-local pixels/patches/images/volumes. Particularly, two similar patches

or sub-volumes can be far from each other within an image, the correlation between their structured noises can be ignored. Thus, Noise2Sim can effectively reduce correlated noise in various real-world applications.

### S3. Estimation of Conditional Discrepancy

Here we aim to empirically estimate the values of the conditional expectation  $\mathbb{E}[\delta_i | s_i + \mathbf{n}_i]$  on the BSD400 dataset, where the standard deviation of Gaussian noise was 25. Specifically, it was estimated with the following equation

$$\hat{\mathbb{E}}[\delta_i | s_i + \mathbf{n}_i] = \frac{1}{M} \sum_{i=1}^M (\hat{\mathbf{x}}'_i - \hat{\mathbf{x}}''_i), \quad [12]$$

where  $\hat{\mathbf{x}}'_i$  and  $\hat{\mathbf{x}}''_i$  are similar image pairs randomly constructed given one of BSD400 images, and  $M$  was set to  $5000 \times 400 = 2 \times 10^6$  (it means each image was repeatedly used 5,000 times), being consistent with the training process. In our experiments, we found that the values of this estimation are closed to zeros, i.e.,  $\hat{\mathbb{E}}[\delta_i | s_i + \mathbf{n}_i] \in [-0.0014, 0.0013]$ , where  $s_i$  was normalized to  $[0, 1]$ . Thus, the zero-mean conditional similarity condition for the Noise2Sim theorem can be well satisfied.

### S4. Implementation of Noise2Sim

#### A. Datasets.

**A.1. Natural Images.** In the subsection of **Application to Natural Images**, we used four publicly available datasets including BSD400 and BSD68 (11) containing grayscale images, BSD500 (37) and Kodak (<http://r0k.us/graphics/kodak/>) containing color images. Specifically, for grayscale images, we used BSD400 that consists of 400  $180 \times 180$  images for training and BSD68 that consists of 68 different sizes of images for testing. For color images, we used BSD500 that consists of 500 different image sizes for training and Kodak that consists of 24 either  $768 \times 512$  or  $512 \times 768$  images for testing. All the above images share the pixel value range of  $[0, 255]$  and were corrupted by two common noise distributions, i.e., Gaussian and Poisson. For Gaussian noise, the noisy images were simply obtained by adding a zero-mean Gaussian noise images with any standard deviations into a clean image. For Poisson noise, the noisy images  $\mathbf{x}_i$  was computed as  $\mathbf{x}_i = \text{Poisson}(s_i/\lambda)/\lambda$ , which is the same as in (19). Note that Poisson noise is conditioned on the clean image, and the mean of noisy images is the corresponding clean image, which means a zero-mean noise.

**A.2. Microscopic Images.** In the subsection of **Application to Microscopic Images**, we used two publicly available Microscopic image datasets, Fluo-C2DL-MSD (MSD) and Fluo-N2DH-GOWT1 (GOWT1), from the Cell Tracking Challenge (<http://celltrackingchallenge.net/2d-datasets/>). These datasets only contain noisy images, and the supervised learning methods cannot be applied. As what was done in (14), only test datasets in MSD and GOWT1 were used for evaluating the denoising algorithms. Specifically, MSD consists of 94 either  $992 \times 832$  or  $1200 \times 782$  grayscale images, half of which were randomly selected for training and the other for testing. GOWT1 consists of 182  $1024 \times 1024$  grayscale images, randomly split for training and testing respectively.

**A.3. Smart Phone Images.** In the subsection S5-E in this SI Appendix, we applied Noise2Sim to reduce the correlated noises on the Smartphone Image Denoising Dataset (SIDD) dataset (38), which were captured under different lighting conditions from 10 scenes. In this study, we selected a small dataset that consists of 8 images from 8 scenes for training and the rest for testing.

**A.4. Low-dose CT Images.** In the subsection of **Application to Low-dose CT Images**, we used the publicly available Mayo dataset for the Low Dose CT (LDCT) Grand Challenge (<https://www.aapm.org/grandchallenge/lowdosect/>). We used the eight patients data for training and the other two for testing. Specifically, the training dataset consists of 4800  $512 \times 512$  slices, and the testing dataset consists of 1136  $512 \times 512$  slices. There are ten patients data, we select two patients (L333 and L506) for testing and the rest as training.

**A.5. Photon-counting Micro-CT Images.** In the subsection of **Application to Spectral CT Images**, we scanned a dead mouse on a MARS spectral CT system, which includes a micro x-ray source and a flat-panel photon-counting detector (PCD). The flat-panel PCD has  $660 \times 124$  pixels, each of which covers an area of  $0.11 \times 0.11 \text{mm}^2$ . The emitting x-ray spectrum at 120kVp is divided into the five energy bins: [7.0 32.0], [32.1 43], [43.1 54], [54.1 70] and [70 120]. The distances between the source to the PCD and object are 310 mm and 210 mm, respectively. In this study, we collected 5,760 views with a translation distance 88.32mm for helical scanning. The number of views for one circle is 720. The voxel size in each energy channel was set to  $0.1 \times 0.1 \times 0.1 \text{mm}^3$ . All reconstructed images were performed using the filtered back-projection method. The reconstruction volume is of  $667 \times 394 \times 394 \times 5$ , i.e., the slice size is  $394 \times 394$ , 667 slices in total, and 5 energy channels in use.

**B. Network Architectures.** In all our experiments, we used a simple two-layer UNet (41) with a residual connection as the denoising network in Noise2Sim, which is the same as that used in (14). In RedCNN (33) and MAPNN (27), specified network architectures are designed for LDCT denoising.

**C. Training Steps.** In fast searching for similar pixels in natural images and microscopic images, we used a publicly available library (<https://github.com/facebookresearch/faiss>), powered by GPU. In all the experiments, we used the same data augmentation strategy as in (14), including random cropping followed by random 90°-rotation and mirroring. The Adam (42) algorithm was coupled with the cosine learning rate schedule (43), with the initial learning rate 0.0005. Our method was implemented on the PyTorch (<https://pytorch.org/>) deep learning platform. The codes have been made available at <https://github.com/niujuangnn/noise2sim>.

### S5. Additional Results

**A. Effects of Patch Size and Neighborhood Range on Denoising Natural Images.** In the Noise2Sim method, searching for an appropriate set of similar pixels is a core task at each reference pixel. In the search, a size-fixed square patch window is translated over a noisy image to find similar pixels. Hence, the patch size, denoted by  $s$ , is a key parameter that affects the accuracy of similarity estimation. The effect of different patch sizes vs. various Gaussian noise levels on PSNR are shown in Table S1. It can be seen that the denoising performance of smaller patch sizes is better for lower noise levels but that of larger patch sizes is better for higher noise levels. This is due to the fact that it requires more contextual information to estimate the similarity accurately when pixels are heavily corrupted by noise.

Moreover, the number of selected similar pixels  $k$  determines the error term  $\delta$  defined in the **Methods** Section in the main text. Then, we evaluated the effect of the number of selected similar pixels on the denoising performance as shown in Table S2. The results show

**Table S1. PSNR results affected by patch size and noise level.**

s \ Std	5	15	25	35	45	55	65	75
3 × 3	33.85	29.90	<b>28.14</b>	<b>26.73</b>	<b>25.73</b>	24.89	24.06	23.45
5 × 5	<b>34.32</b>	<b>29.98</b>	28.02	26.72	25.69	24.93	24.03	23.45
7 × 7	33.13	29.87	27.93	26.70	25.67	24.83	24.02	<b>23.74</b>
11 × 11	32.10	29.82	27.43	26.56	25.69	24.86	<b>24.25</b>	23.71
15 × 15	31.97	28.96	27.58	26.53	25.67	<b>24.94</b>	24.18	23.68

**Table S2. PSNR results affected by the number of similar pixels and the patch size, for Gaussian noise of  $Std = 25$ .**

s \ k	2	4	8	16	32	64
3 × 3	26.93	27.90	<b>28.15</b>	28.08	27.95	27.01
5 × 5	26.95	27.84	<b>28.02</b>	26.24	26.55	25.94
7 × 7	26.91	27.68	<b>27.93</b>	27.71	27.50	27.28
11 × 11	26.81	<b>27.58</b>	27.43	27.23	25.21	25.02
15 × 15	26.78	27.15	<b>27.58</b>	26.57	26.47	24.76

that the best denoising performance was generally associated with  $k = 8$  in our study. These results suggest that there is a trade-off between the error term and the number of training samples. Specifically, increasing the number of similar pixels will increase  $\delta$  values, while decreasing this number will increase the noise residual in the denoised image. A good balance is  $k = 8$  in our experiments.

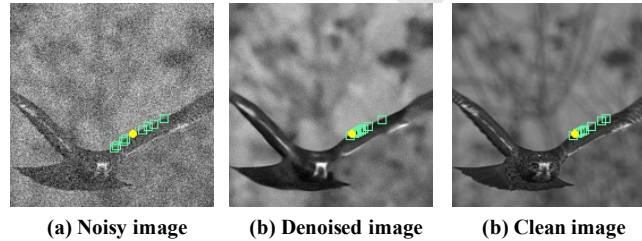


**Fig. S3.** Distribution of similar patches in (a) an original noisy image, (b) the denoised image, and (c) the clean image.

**B. Effects of Iterative Training Cycles on Denoising Natural Images.** Any estimate of similarity between image patches is necessarily compromised in a noisy image, such an estimate may be improved in a denoised image produced by a trained denoising model. That is, the Noise2Sim idea can be repeatedly applied to refine the resultant denoising model. By doing so, the similarity measures can be gradually improved, leading to a superior denoising performance. Fig. S3 shows the change in the distribution of similar image patches after one iteration, and the distribution in the denoised image is very close to that in the clean image. We also evaluated the iterative training by computing the similarity measures in reference to the clean image. Table S3 shows that the iterative training enhances the denoising performance, especially when noise level is small. When the images are severely corrupted, the initial denoising results are not good enough. As a result, iterative training might compromise the estimation of similar pixels.

**C. Methods for Pairing Natural Image Pixels.** Given a set of  $k + 1$  similar images as described in Subsection S1-A, there are four reasonable methods for pairing them: 1) Pair the original noisy image as the input to its randomly constructed similar image as the target; 2) reverse the input and label used in 1); 3) pair two of  $k$  sorted similar images without pixel-wise randomization; and 4) pair similar images that were randomly and independently constructed pixel-wise. The results in Table S4 demonstrate that the fourth pairing method achieves the best denoising performance. The reason seems that, in the fourth pairing implementation, we use two randomly reconstructed images, which are  $s_i + \delta'_i + n_i$  and  $s_i + \delta_i + \hat{n}_i$ , to train a denoising network, instead of using  $s_i + n_i$  and  $s_i + \delta_i + \hat{n}_i$  as stated in the Noise2Sim theorem. Actually, they are equivalent as both of them are paired similar images. Let  $\hat{s}_i = s_i + \delta'_i$ , then the randomly reconstructed pairs can be rewritten as  $\hat{s}_i + n_i$  and  $\hat{s}_i + \delta''_i + \hat{n}_i$ , where  $\delta''_i = \delta_i - \delta'$ . We can verify that  $E[\hat{n}_i | \hat{s}_i + n_i] = 0$  and  $E[\delta''_i | \hat{s}_i + n_i] = 0$ , and the Noise2Sim Theorem remains true. The advantage of such an implementation is that the capacity of possible image pairs can be significantly increased from  $(k + 1)^{HW}$  to  $(k + 1)^{2HW}$ , leading to a better performance.

**D. Natural Images with Independent Noise.** Here we conducted more experiments for comparing Noise2Sim with current denoising methods. We used the same datasets and network architecture as those in the Noise2Void work (14). Specifically, we first compared Noise2Sim with Noise2Clean, Noise2Noise (13), Noise2Void (14), and NLM (8) methods on commonly used BSD68 and BSD400 (11), BSD500 (37) and Kodak datasets, which were corrupted by either Gaussian or Poisson noises. Here the standard deviation (Std) of Gaussian noise was set to 25 (the image value range is  $[0, 255]$ ), and the parameter of Poisson noise to  $\lambda = 30$ ; please refer to SI for more details. The mean PSNR and SSIM results on whole datasets are in Table S5, which indicates that Noise2Sim is better than the NLM and Noise2Void methods. The visual results are shown in Fig. S4, where each row presents the results obtained using one of the compared methods on a specific image. These results indicate that the Noise2Sim method can effectively remove additive Gaussian noises and conditional Poisson noises

**Table S3. PSNR results after iterative training at different noise levels (Std from 5 to 65).**

Std	5	15	25	35	45	55	65
<i>W/O</i>	33.85	29.90	28.14	26.73	25.73	24.89	24.06
<i>With</i>	34.15	30.25	28.27	26.98	25.75	24.88	24.02
<i>Upper</i>	34.22	30.54	28.60	27.14	26.08	25.15	24.33

**Table S4. Results obtained using different methods for pairing similar pixels in patches of  $3 \times 3$  for  $k = 8$  and Gaussian noise Std 25.**

Pairing Method	1	2	3	4
PSNR	27.12	27.78	27.48	<b>28.15</b>

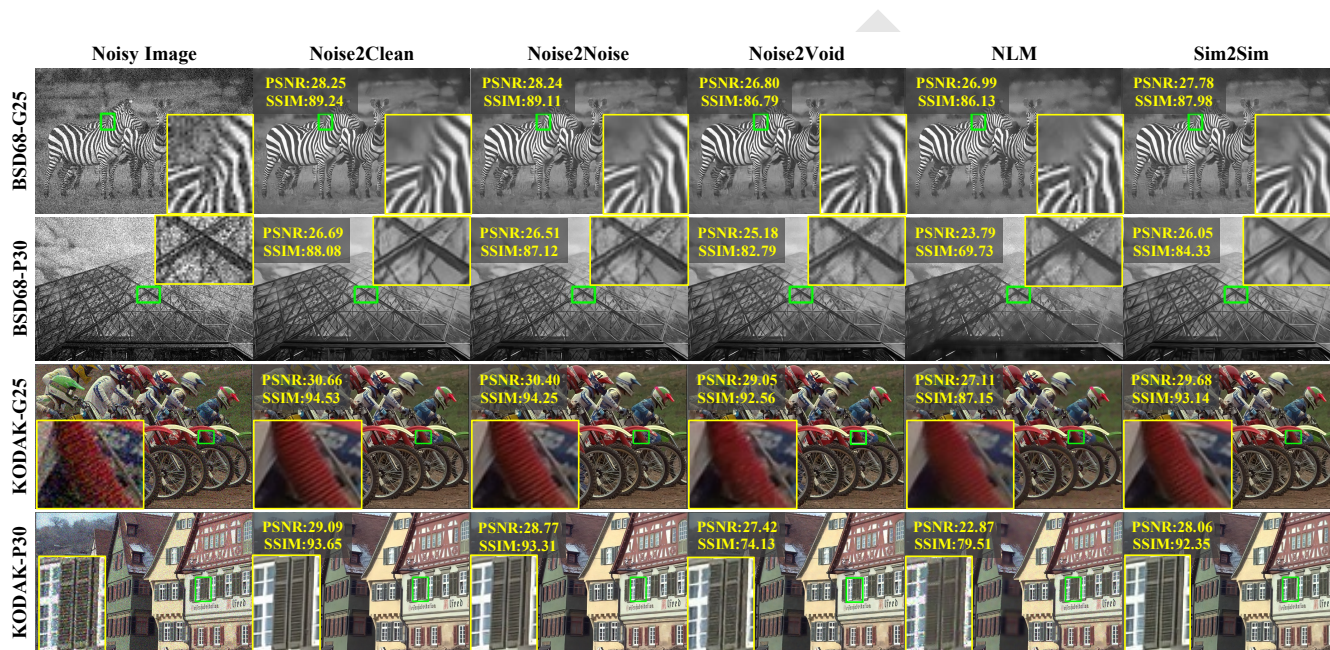


**Fig. S4.** Visual comparison of denoising results on different datasets, where *G25* means Gaussian noise with  $Std = 25$ , and *P30* means Poisson noise with  $\lambda = 30$ . The PSNR and SSIM values are included.

**Table S5. Comparison of denoising results using different methods on representative datasets, where PSNR and SSIM(%) values were reported.**

Dataset	Noise2Clean	Noise2Noise	Noise2Void	Noise2Sim
BSD68-G25	28.96/89.78	28.88/89.44	27.72/86.65	28.27/88.17
BSD68-P30	28.08/88.26	27.98/87.78	27.08/85.24	27.37/85.70
Koak-G25	32.45/94.23	31.68/93.75	31.02/92.48	31.18/92.52
Koak-P30	31.74/93.65	31.52/93.41	30.35/91.34	30.44/91.56

in gray-scale and color images. In consistent with the numerical results in Table S5, the visual results show that Noise2Sim is consistently better than the NLM and Noise2Void counterparts. The PSNR and SSIM values of individual images also support these findings.

**Table S6. Comparison results in terms of PSNR, SSIM, and runtime obtained using different methods on BSD68 with additive Gaussian noise of Std 25.**

Method	BM3D	NLM	SNT	N2Void	N2Self	N2Same	N2Sim
PSNR	28.59	27.58	27.22	27.72	27.07	28.02	28.27
SSIM(%)	88.26	85.27	83.06	86.65	87.36	87.18	88.17
Runtime(s)	3.32	0.43	141.87	0.001	0.002	0.002	0.001

In Table S6, we compared Noise2Sim with more relevant methods in terms of PSNR and inference time, including BM3D (10), Noise2Self (15), Noise2Same (16), and SNT (18) methods. Noise2Sim has the same inference time as Noise2Clean, Noise2Noise, and Noise2Void, directly taking the noisy image as input and outputting the denoised image without any additional processing. Noise2Self and Noise2Same take a little longer inference time as their networks are deeper than Noise2Void and Noise2Sim. During training, Noise2Sim requires extra time to pre-compute similar images as compared with Noise2Clean and Noise2Noise that assume target images available in the first place. Nevertheless, this pre-processing time is very short (about 18 seconds for BSD400 dataset) relative to the network training time (several hours). On the other hand, Noise2Sim achieves better results than other unsupervised deep denoising methods. Although the classic BM3D method achieves the results comparable to the Noise2Sim counterparts, its inference time is thousands times of that taken by Noise2Sim, which is consistent with what was reported in the Noise2Void (14) paper. Therefore, Noise2Sim is both effective and efficient.

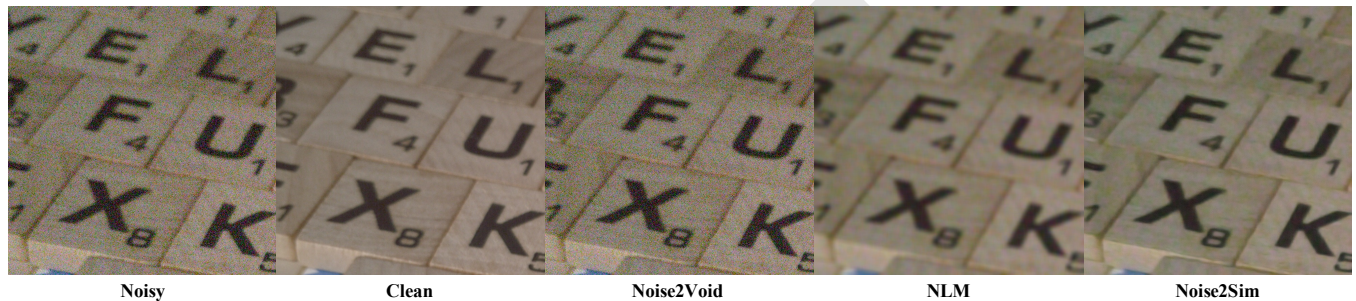


**Fig. S5.** Denoising results of different methods on 2D smartphone images.

**E. Smart Phone Images with Correlated Noise.** Here we applied Noise2Sim to the smart phone image denoising using the searching algorithm in subsection S1-B on the SSID dataset described in subsection S4-A.3. The visual results are shown in Fig. S5. Due these real-world noises are correlated, Noise2Void method cannot work, while traditional NLM method produced over-smoothed results. In contrast, Noise2Sim achieved significantly better results, demonstrating that Noise2Sim has the ability to remove correlated noises in 2D images using single noisy images only.

**Table S7. Denoising results with different k on the Mayo dataset, where N2S-k{a} means the Noise2Sim with  $k = a$ . N2S-S2 means only  $(i - 2)^{th}$  and  $(i + 2)^{th}$  slices are used as the similar targets for  $i^{th}$  slice.**

Dataset	N2S-k1	N2S-k2	N2S-S2	N2S-k3	N2S-k4
PSNR	27.91	<b>28.21</b>	<u>27.53</u>	27.94	27.73
SSIM	90.17	<b>90.22</b>	<u>88.24</u>	89.67	89.18

**F. Low-dose CT Images.** As discussed in the main text, the noise dependence of similar pixels becomes weaker but self-similarity could become less with increasing the searching range parameter of  $k$ . Here we evaluated the performance of Noise2Sim using different  $k$ . As shown in Table S7,  $k = 2$  achieves the best trade-off between noise independence and self-similarity. In addition, when we only use the  $(i - 2)^{th}$  and  $(i + 2)^{th}$  slices as similar targets for  $i^{th}$  slice without including the nearest neighbors, the performance is obviously degraded. This is because the accurate similar information in the nearest neighbors is important for noise suppression, although containing weakly correlated noises. In this study, the performance is evaluated based on the normal-dose CT that still contain some noises. Thus, parameter  $k$  can be set according to the preference in specific applications.

**G. Photon-counting Micro-CT Images.** As described in Subsection **Application to Spectral CT Image**, both Noise2Sim and BM3D have the ability to control the denoising level. Here we give a comprehensive visual comparison between Noise2Sim and BM3D methods under different denoising levels, as shown in Fig. S7. It can be seen that BM3D for a small denoising level generated severe structured artifacts, especially in the  $5^{th}$  energy bin with strong noise. On the other hand, BM3D for a large denoising level over-smoothed image details. In contrast, Noise2Sim can remove more noise by increasing the neighborhood parameter  $k$ , and does not produce any artifacts

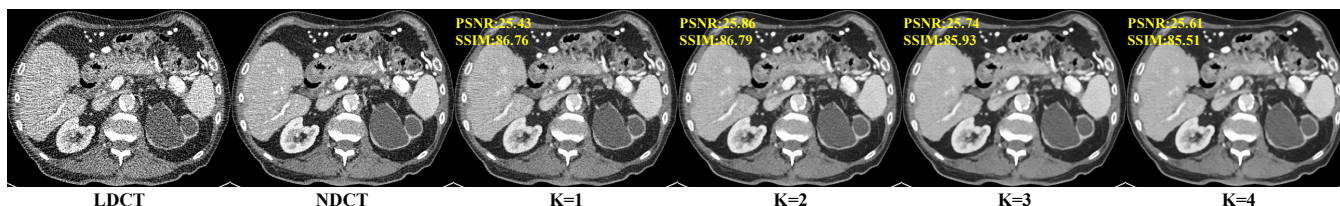


Fig. S6. Noise2Sim results obtained at different denoising levels on the Mayo dataset.

and well preserves structural details. Even for  $k = 10$ , the subtle structures are still clear in the Noise2Sim results, without being overly smoothed as shown in the BM3D results.

1. M Lindenbaum, M Fischer, A Bruckstein, On gabor's contribution to image enhancement. *Pattern Recognit.* **27**, 1 – 8 (1994).
2. P Perona, J Malik, Scale-space and edge detection using anisotropic diffusion. *IEEE Transactions on Pattern Analysis Mach. Intell.* **12**, 629–639 (1990).
3. F Catté, PL Lions, JM Morel, T Coll, Image selective smoothing and edge detection by nonlinear diffusion. *SIAM J. on Numer. Analysis* **29**, 182–193 (1992).
4. LP Yaroslavsky, Digital picture processing - an introduction. *Springer Verlag* (1985).
5. SM Smith, JM Brady, SUSAN-A New Approach to Low Level Image Processing. *Int. J. Comput. Vis.* **23**, 45–78 (1997).
6. C Tomasi, R Manduchi, Bilateral filtering for gray and color images in *ICCV*. pp. 839–846 (1998).
7. G Yu, G Sapiro, DCT Image Denoising: a Simple and Effective Image Denoising Algorithm. *Image Processing On Line* **1**, 292–296 (2011).
8. A Buades, B Coll, J Morel, A non-local algorithm for image denoising in *CVPR*. Vol. 2, pp. 60–65 vol. 2 (2005).
9. L Chiron, MA van Agthoven, B Kieffer, C Rolando, MA Delsuc, Efficient denoising algorithms for large experimental datasets and their applications in fourier transform ion cyclotron resonance mass spectrometry. *Proc. Natl. Acad. Sci.* **111**, 1385–1390 (2014).
10. K Dabov, A Foi, V Katkovnik, K Egiazarian, Image denoising by sparse 3-d transform-domain collaborative filtering. *IEEE Transactions on Image Process.* **16**, 2080–2095 (2007).
11. K Zhang, W Zuo, Y Chen, D Meng, L Zhang, Beyond a gaussian denoiser: Residual learning of deep cnn for image denoising. *IEEE Transactions on Image Process.* **26**, 3142–3155 (2017).
12. C Tian, et al., Deep learning on image denoising: An overview. *Neural Networks* **131**, 251–275 (2020).
13. J Lehtinen, et al., Noise2Noise: Learning image restoration without clean data in *ICML*. Vol. 80, pp. 2965–2974 (2018).
14. A Krull, T Buchholz, F Jug, Noise2void - learning denoising from single noisy images in *CVPR*. pp. 2124–2132 (2019).
15. J Batson, L Royer, Noise2Self: Blind denoising by self-supervision in *ICML*. Vol. 97, pp. 524–533 (2019).
16. Y Xie, Z Wang, S Ji, Noise2Same: Optimizing a self-supervised bound for image denoising in *NeurIPS*. Vol. 33, pp. 20320–20330 (2020).
17. A Krull, T Vičar, M Prakash, M Lalit, F Jug, Probabilistic noise2void: Unsupervised content-aware denoising. *Front. Comput. Sci.* **2**, 5 (2020).
18. A Khodja, Z Zheng, Y He, Similarity noise training for image denoising. *Math. Comput. Sci.* **5**, 56–63 (2020).
19. S Laine, T Karras, J Lehtinen, T Aila, High-quality self-supervised deep image denoising in *NeurIPS*. pp. 6970–6980 (2019).
20. C Broaddus, A Krull, M Weigert, U Schmidt, G Myers, Removing structured noise with self-supervised blind-spot networks in *International Symposium on Biomedical Imaging*. pp. 159–163 (2020).
21. V Lempitsky, A Vedaldi, D Ulyanov, Deep image prior in *CVPR*. pp. 9446–9454 (2018).
22. Y Quan, M Chen, T Pang, H Ji, Self2self with dropout: Learning self-supervised denoising from single image in *CVPR*. (2020).
23. J Harte, A Kinzig, J Green, Self-similarity in the distribution and abundance of species. *Science* **284**, 334–336 (1999).
24. C Niu, G Wang, Noise2sim – similarity-based self-learning for image denoising. *2011.03384 v1* (2020).
25. X Li, G Zhang, J Wu, et al., Reinforcing neuron extraction and spike inference in calcium imaging using deep self-supervised denoising. *Nat. Methods* (2021).
26. Z Zhang, X Liang, W Zhao, L Xing, Noise2context: Context-assisted learning 3d thin-layer for low-dose ct. *Med. Phys.* (2021).
27. H Shan, et al., Competitive performance of a modularized deep neural network compared to commercial algorithms for low-dose ct image reconstruction. *Nat. Mach. Intell.* **1**, 269–276 (2019).
28. J Chen, et al., Three-dimensional residual channel attention networks denoise and sharpen fluorescence microscopy image volumes. *Nat. Methods* **18**, 678–687 (2021).
29. A Horé, D Ziou, Image quality metrics: Psnr vs. ssim in *ICPR*. pp. 2366–2369 (2010).
30. Z Wang, A Bovik, H Sheikh, E Simoncelli, Image quality assessment: from error visibility to structural similarity. *IEEE Transactions on Image Process.* **13**, 600–612 (2004).
31. A Berrington de González, et al., Projected Cancer Risks From Computed Tomographic Scans Performed in the United States in 2007. *Arch. Intern. Medicine* **169**, 2071–2077 (2009).
32. G Wang, A perspective on deep imaging. *IEEE Access* **4**, 8914–8924 (2016).
33. H Chen, et al., Low-dose ct with a residual encoder-decoder convolutional neural network. *IEEE Transactions on Med. Imaging* **36**, 2524–2535 (2017).
34. V Sreeram, P Agathoklis, On the properties of gram matrix. *IEEE Transactions on Circuits Syst. I: Fundamental Theory Appl.* **41**, 234–237 (1994).
35. W Wu, et al., Deep learning based spectral ct imaging. *Neural Networks* (2021).
36. S A, N S, Spectral computed tomography: Fundamental principles and recent developments. *Korean journal radiology* **22**, 86–96 (2021).
37. P Arbelaez, M Maire, C Fowlkes, J Malik, Contour detection and hierarchical image segmentation. *IEEE Trans. Pattern Anal. Mach. Intell.* **33**, 898–916 (2011).
38. A Abdelhamed, S Lin, MS Brown, A high-quality denoising dataset for smartphone cameras in *CVPR*. (2018).
39. V Ulman, An objective comparison of cell-tracking algorithms. *Nat. Methods* **14**, 1141–1152 (2017).
40. D Wu, K Gong, K Kim, X Li, Q Li, Consensus neural network for medical imaging denoising with only noisy training samples in *MICCAI 2019*. (2019).
41. O Ronneberger, P Fischer, T Brox, U-net: Convolutional networks for biomedical image segmentation in *MICCAI*, eds. N Navab, J Hornegger, WM Wells, AF Frangi. pp. 234–241 (2015).
42. DP Kingma, J Ba, Adam: A method for stochastic optimization in *ICLR*, eds. Y Bengio, Y LeCun. (2015).
43. I Loshchilov, F Hutter, Sgdr: Stochastic gradient descent with warm restarts in *ICLR*. (2017).

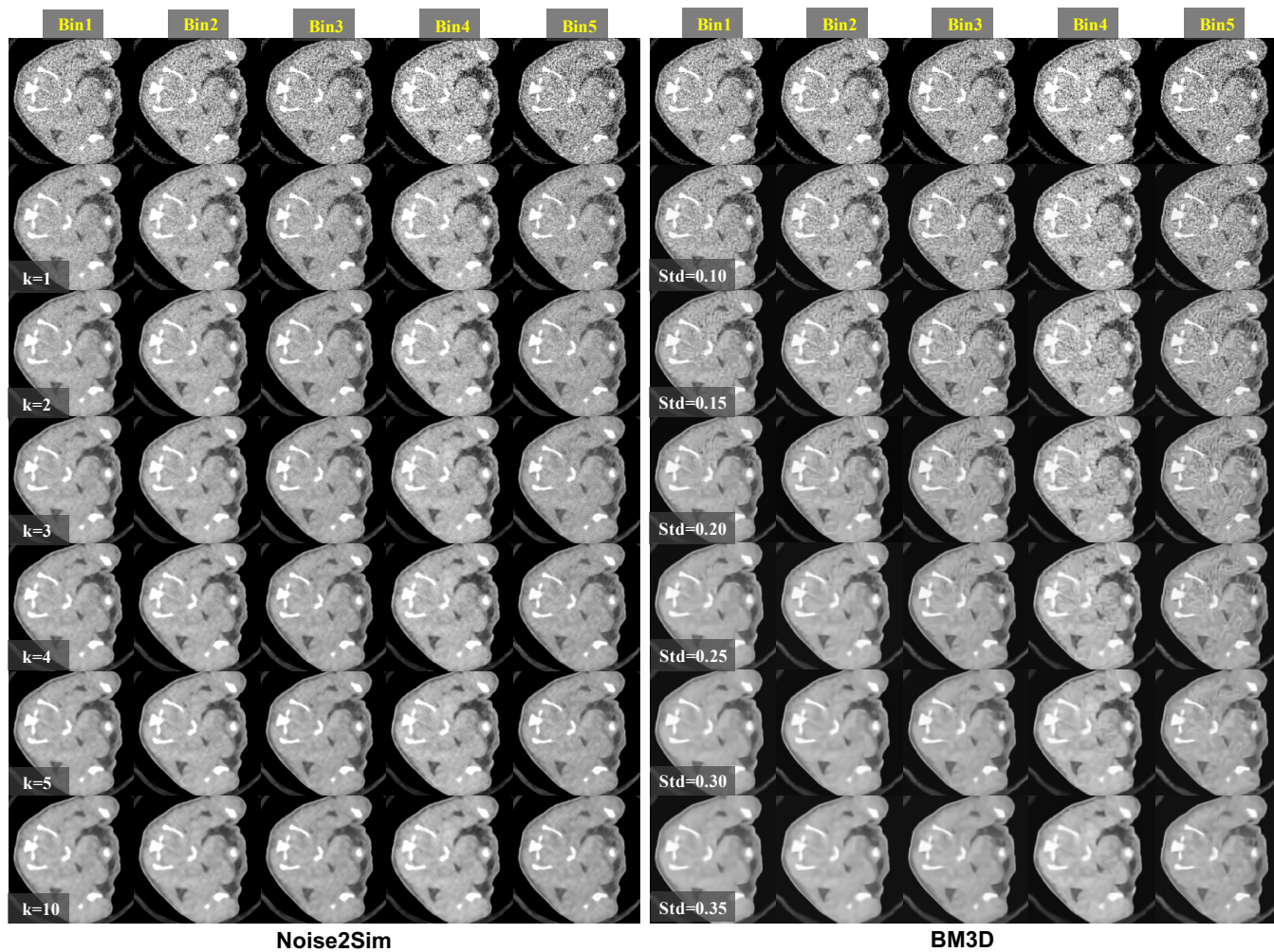


Fig. S7. Noise2Sim and BM3D results on 4D spectral CT images obtained at different denoising levels.